DØ Note 6347-CONF

Updated search for the Standard Model Higgs Boson in Final States with three Leptons and missing transverse energy with 9.7 fb^{-1} of $p\bar{p}$ collisions at $\sqrt{s} = 1.96$ TeV

The DØ Collaboration
URL http://www-d0.fnal.gov
(Dated: June 30, 2012)

A search for the standard model (SM) Higgs boson is presented based on a sample of events with three identified leptons, using electrons and muons in the $ee\mu$ and $\mu\mu e$ final states, produced in $p\bar{p}$ collisions at $\sqrt{s} = 1.96$ TeV. Data collected from April 2002 to September 2011 by the RunII DØ detector corresponds to 9.7 fb^{-1} of integrated luminosity. No excess is observed above the SM background and limits are extracted on the SM Higgs boson production cross section for Higgs boson masses between 100 and 200 GeV.

Preliminary Results for Summer 2012 Conferences

I. INTRODUCTION

At the Tevatron, associated production of $q\bar{q} \to WH$ and $q\bar{q} \to ZH$ have some of the highest cross section production rates for final states containing a SM Higgs boson, second only to gluon-gluon fusion Higgs boson production. Furthermore, since the $H \to WW$ decay modes dominate the branching ratios of the Higgs boson in the standard model (SM) for Higgs boson masses above $m_H = 135$ GeV, this makes $VH \to VWW$ (where V is either a W or a Z boson) a promising process to use to search for the Higgs boson. The hadronic decays of the W bosons have high branching fractions, but suffer from a large hadronic background that is difficult to separate from the signal. Despite having a low 31.4%(10.2%) branching fraction, the leptonic decays of the $W(Z)$ bosons provide a more sensitive final state search at the Tevatron. The $H \to WW \to \ell\nu\ell\nu$ decay suffers from a large $Z \to \ell\ell$ background. By requiring a third lepton, this background becomes more manageable. Contributions from gluon fusion Higgs boson production decaying via $H \to ZZ$ are significant in the trilepton final states and are included in the signal modeling, along with the less significant $gg \to H \to WW$ process and vector boson fusion $VV \to H$ production.

We present a search for the Higgs boson with a final state containing at least three isolated leptons, either electrons or muons, and missing transverse momentum − defined as the energy imbalance in the transverse plane ($\not\!\!E_T$). Due to the better sensitivity and lower backgrounds, we focus on the $ee\mu$ and $\mu\mu e$ final states. This analysis was performed on the full Run II dataset recorded between April 2002 and September 2011, corresponding to 9.7 fb^{-1} of integrated luminosity.

In this update, we have loosened our selection cuts in the $\mu\mu e$ final state and split the events of that final state into three subsets, defined below. These changes allows us to be more sensitive to specific signal inputs (WH, ZH, and $H \to ZZ$ when setting limits.

II. DØ DETECTOR

This analysis is based on data collected at the multi-purpose DØ detector [1]. The relevant components of the DØ detector are described below. The central-tracking system consists of a silicon microstrip tracker (SMT) and a central fiber tracker (CFT), both contained within a 2 T superconducting solenoidal magnet. The SMT has $\approx 800,000$ individual strips, with typical pitch of $50 - 80$ μm, and a design optimized for tracking and vertexing capability at pseudorapidities of $|\eta| < 2.5$. Here we define $\eta = -ln(tan\ \theta/2)$, where θ is the polar angle relative to the proton beam direction. The SMT has a six-barrel longitudinal structure, each with a set of four layers arranged axially around the beam pipe, and interspersed with 16 radial disks. A new layer of silicon sensors (Layer 0) was added just outside the beam pipe in 2006 to improve vertexing [2]. The CFT has eight concentric coaxial barrels, each consisting of two doublet layers of overlapping scintillating fibers. The inner-most double layer is parallel to the collision axis, while the second alternates by $\pm 3^\circ$ relative to the axis.

Central and forward preshower detectors are located just outside of the solenoid, but before the calorimetry, to help measure the energy loss associated with particles traveling through the solenoid material. The calorimetry system consists of three liquid-argon sampling calorimeters: a central section (CC) covering $|\eta|$ up to ≈ 1.1, and two end calorimeters (EC) that extend coverage to $|\eta| \approx 4.2$, housed in separate cryostats [3]. In an attempt to include the intercryostat region (ICR) where there is incomplete calorimeter coverage, scintillators between the CC and EC provide sampling of developing showers at $1.1 < |\eta| < 1.4$.

A muon system resides beyond the calorimeters, and consists of a layer of tracking detectors and scintillation trigger counters before 1.8 T toroids, followed by two similar layers after the toroids [4]. Tracking at $|\eta| < 1$ relies on 10 cm wide drift tubes [3], while 1 cm mini-drift tubes are used at $1 < |\eta| < 2$.

Luminosity is measured with two arrays of 24 plastic scintillator counters each, located in front of the EC cryostats ($2.7 < |\eta| < 4.4$), using a method that relies on counting the number of beam crossings with zero interactions. Trigger and data acquisition systems are designed to accommodate the high luminosities of Run II. Based on preliminary information from all three sub-systems, the output of the first level of triggering is used to limit the rate for accepted events to approximately 1.5 kHz. At the next trigger stage, with more refined information, the rate is reduced further to ≈ 0.8 kHz. These first two levels of triggering rely mainly on hardware and firmware. The third and final level of the trigger, with access to all the event information, uses software algorithms and a computing farm to make decisions, and further reduces the output rate to ≈ 100 Hz, which is then written to tape.

III. DATA AND MONTE CARLO SAMPLES

The data sample used in this analysis was collected between April 2002 and September 2011 (Run II), and corresponds to an integrated luminosity of 9.7 fb^1 for the trilepton final state after imposing data quality requirements.

To maximize our signal acceptance, we use all events collected by DØ that pass our event selection without requiring a specific trigger to have collected the event. The simulated background samples are normalized to the integrated luminosity and appropriate cross sections. Cross sections for Higgs boson production and decay branching fractions for each mass point are listed in [5].

The signal and WW, WZ, and ZZ diboson SM backgrounds have been generated using PYTHIA [6]. The $Z/\gamma*$ + jets, W + jets and $t\bar{t}$ backgrounds are modeled using ALPGEN [7], with PYTHIA used to model the jet hadronization. The $Z/\gamma*$ boson p_T is reweighted to match the distribution seen in data [8]. The W + jets background is found to be completely negligible, and is dropped from our modeling. All of the MC is passed through a GEANT [9] simulation of the DØ detector. The $Z/\gamma*$ and diboson production cross sections are normalized to next-to-leading order (NLO) calculations from MCFM [10]. The $t\bar{t}$ background is normalized to an approximate next-to-next-NLO cross section calculation[11]. We overlay data events from random beam crossings onto the MC events to simulate the effects of multiple interactions and of noise in the detector.

IV. OBJECT AND EVENT SELECTION

Electrons are reconstructed using information from the calorimetry and tracking systems. Electromagnetic (EM) showers are identified in the calorimeter by comparing the longitudinal and transverse shower profiles to those of simulated electrons. The fraction of energy deposited in the EM layers, compared to the total energy deposited in the calorimetry system, must be greater than 90%. A shower must be isolated, as measured from the calorimeter energy information, have a transverse momentum (p_T) greater than 10 GeV, and be within the acceptance of the calorimeter ($|\eta| < 1.1$ in the CC or $1.5 < |\eta| < 2.5$ in the EC). Neutral Network outputs and an electron likelihood are used to further separate electrons from hadronic showers. To help reduce the photon background contribution, the shower must be matched to a track found in the central tracker. In the CC region, it is also required that the ratio of the cluster's energy to the track's transverse momentum ($E_T^{cluster}/p_T^{track}$) be less than eight. Due to less precise energy resolutions, electrons reconstructed in the ICR are not considered. All other electrons are kept.

For the $\mu\mu e$ final state, we model the $Z + \gamma$ background using a data driven method, which takes events where the photon is correctly reconstructed and uses them to model events where the photon fakes an electron. Like electrons, photons are reconstructed using information from the calorimetry and tracking systems. The EM shower is reconstructed in the calorimeter with an EM fraction greater than 90%, with similar calorimeter isolation and detector η cuts as those used to reconstruct electrons. A Neutral Network is also used to distinguish photons from jets. The most significant difference between the electron and photon reconstruction is in the tracker; we require that there be no track pointing to the photon. We estimate the $\gamma \to e$ fake ratio using events with two identified muons and a photon with $\not\!\!E_T < 20$ GeV and a $\mu\mu\gamma$ invariant mass between 75 and 105 GeV. This kinematic region is dominated by $Z \to \mu\mu$ decays with final state photon radiation, and we take the ratio of the number of events reconstructed as photons to that reconstructed as electrons as our fake ratio. We then apply this fake ratio to data $\mu\mu\gamma$ events outside this region to estimate the $\mu\mu\gamma \to \mu\mu e$ background.

Muon tracks are reconstructed from hits in the wire chambers and scintillators in the muon system. The muon tracks then must be matched to tracks in the central tracker with transverse momentum greater than 10 GeV. Muon reconstruction is restricted to the coverage of the muon system, $|\eta| < 2.0$. The distance of closest approach of the matched central track to the beamline in plane transverse to the beamline, dca, must satisfy the requirement $|dca| <$ 0.04(0.2) cm for tracks with(no) SMT hits. This matched track in the central tracker must also have a reconstruction χ^2 per degrees of freedom less than 9.5 and at least two CFT hits. To identify isolated muons, the scalar sum of the transverse momenta of all the tracks inside a $\Delta\mathcal{R} < 0.5$ cone around the matched muon track with the exception of the matched muon track itself must be less than $0.2\times p_T^{\mu}$. Here we defined $\Delta\mathcal{R} = \sqrt{(\Delta\phi)^2 + (\Delta\eta)^2}$, where ϕ is the azimuthal angle. Similarly, the scalar sum of the transverse energies of all calorimeter deposits inside a hollow cone $0.1 < \Delta\mathcal{R} < 0.4$ around the muon must be less than $0.2\times p_T^{\mu}$. These scaled isolation requirements are used to help reject low$-p_T$ muons from heavy flavor decays and maximize the efficiency of high$-p_T$ prompt muons. Cosmic ray muons are suppressed by requiring a timing criterion on the hits in the scintillator layers.

We use jet information in the $\mu\mu e$ final state to help distinguish signal from background. Jets are reconstructed from energy deposits found within the CC and EC calorimeters using the RunII midpoint cone algorithm [12] with a cone size of $dR = 0.5$. Jets are required to have a $p_T > 15$ GeV and a detector eta acceptance of $|\eta_{det}| < 2.4$. The jets in both data and MC have the standard jet energy scale (JES) applied [13]. Jets that have at least two tracks within $\Delta\mathcal{R}$(track,jet-axis) ≤ 0.5 are considered to be vertex confirmed. We see that distributions with and without vertex requirements are well modeled, so we consider jets both with and without vertex confirmation. We only consider vertex confirmed jets with a $p_T > 20$ GeV; (vertex confirmed jets with a p_T between 15 and 20 GeV will still be in the inclusive jet sample). We require the electron and jet be separated by $\Delta\mathcal{R} > 0.5$, and that the muons and jets be separated by $\Delta\mathcal{R} > 0.1$; the muon isolation criteria rejects most muons within $\Delta\mathcal{R} < 0.4$ of a jet.

Samples	$ee\mu$	$\mu\mu e$		
	final	non-Z	$Z + \not\!\!E_T{}^{significance}$	Z + no $\not\!\!E_T{}^{significance}$
Data	96	45	57	119
Signal	1.39	0.47	0.38	0.25
WH	0.55	0.34	0.12	0.03
ZH	0.57	0.10	0.24	0.16
HZZ	0.26	0.04	0.02	0.06
HWW	0.01	< 0.01	< 0.01	< 0.01
VBF	< 0.01	< 0.01	< 0.01	< 0.01
Total Background	89.20 ± 2.36	51.04 ± 1.64	54.77 ± 1.35	124.56 ± 2.44
$Z \to ee + jets$	48.26 ± 2.23	–	–	–
$Z \to \mu\mu + jets$	–	14.09 ± 1.05	8.61 ± 0.78	32.25 ± 1.46
$Z \to \tau\tau + jets$	4.33 ± 0.64	0.34 ± 0.10	0.17 ± 0.11	< 0.01
$Z\gamma$	–	33.37 ± 1.25	26.43 ± 1.09	82.95 ± 1.95
WZ	23.45 ± 0.35	1.70 ± 0.04	17.30 ± 0.13	4.65 ± 0.08
ZZ	11.09 ± 0.16	0.75 ± 0.04	1.95 ± 0.07	4.62 ± 0.11
WW	0.69 ± 0.13	0.23 ± 0.05	0.05 ± 0.02	0.03 ± 0.02
$t\bar{t}$	1.38 ± 0.07	0.54 ± 0.04	0.26 ± 0.03	0.06 ± 0.02

TABLE I: Expected yields for $m_H = 145$ GeV for the complete RunII dataset. Uncertainties shown are based only on the statistical uncertainties on the number of generated background events.

The missing transverse energy, $\not\!\!E_T$, is obtained from a vector sum of the transverse components of calorimeter energy depositions and corrected for identified muons. Modified MET variables, $\not\!\!E_T{}^{special}$ and $\not\!\!E_T{}^{significance}$, are used to discriminate events with real $\not\!\!E_T$ from events where the $\not\!\!E_T$ arises from mismeasurement. The $\not\!\!E_T{}^{special}$ variable assigns less significance to the missing energy in an event when the opening angle, $\Delta\phi$, between the $\not\!\!E_T$ and any other lepton or jet is small, as this may be a potential source of mismeasurement. The $\not\!\!E_T{}^{special}$ is defined as follows: $\not\!\!E_T$ if $\Delta\phi(\not\!\!E_T, \text{nearest lepton/jet}) > \pi/2$ or $\not\!\!E_T \times \sin(\Delta\phi(\not\!\!E_T, \text{nearest lepton/jet}))$ otherwise. A $\not\!\!E_T{}^{significance}$ is the difference, expressed in standard deviations expected resolutions of the objects in the event projected along the $\not\!\!E_T$direction, between the measured $\not\!\!E_T$ and 0. The value of the standard deviation used is based on the expected resolutions of the physics objects in the event projected along the $\not\!\!E_T$direction.

The transverse mass is defined as $M_T = \sqrt{2 \cdot p_T^{\ell} \cdot \not\!\!E_T \cdot (1 - cos\Delta\phi(\ell, \not\!\!E_T))}$, and the minimum transverse mass between the two same flavor leptons is defined as $M_T^{min} = min(M_T(\ell_1, \not\!\!E_T), M_T(\ell_2, \not\!\!E_T))$.

We select events with three isolated, highly-energetic leptons (two of the same flavor - ℓ_1, ℓ_2, while the third is not - ℓ_3'). In both channels the transverse momenta must satisfy $p_T^{\ell_1} > 15$ GeV, $p_T^{\ell_2} > 10$ GeV, and $p_T^{\ell_3'} > 10$ GeV. In addition, the same flavor dilepton invariant mass is required to be greater than 15 GeV. To ensure that the leptons originate from $p\bar{p}$ collision, we require that their position along the beamline at the distance of closest approach to the interaction point, z_{dca}, be less than 3 cm from the other 2 leptons. An additional cut is made in the $ee\mu$ channel where the minimal z_{dca} distance between the muon and either of the two electrons must be less than 1 cm. This is to help remove muons produced by other collisions in the event or cosmic rays. We currently do not search in eee or $\mu\mu\mu$ final states, focusing on mixed flavor events which have a larger signal acceptance.

We divide the $\mu\mu e$ anaylsis into three sub-channels. The non-Z subchannel has a di-muon invariant mass of less than 60 GeV or more than 130 GeV, as well as any events with two like-sign muons. The $Z + \not\!\!E_T{}^{significance}$ subset contains events with oppositely charged muons, a di-muon invariant mass between 60 and 130 GeV, and $\not\!\!E_T{}^{significance} > 2.0$. The Z + no $\not\!\!E_T{}^{significance}$ contains the remaining events in the Z mass region with $\not\!\!E_T{}^{significance} \leq 2.0$ We make this split to separate our signal into different types; the non-Z subset is dominated by WH events, the $Z + \not\!\!E_T{}^{significance}$ subset is dominated by ZH production, and the Z + no $\not\!\!E_T{}^{significance}$ is dominated by ZH production and $H \to ZZ$ decays.

The $\mu\mu e$ final state requires the additional condition that there be one and only one electron in the event, as to not overlap with the $ee\mu$ channel.

The final $ee\mu$ and $\mu\mu e$ yields for $m_H = 145$ GeV are shown in Table I.

V. FINAL DISCRIMINANTS

In the last step of the event selection, the signal is separated from the remaining background using a gradient boosted decision tree (BDT) technique for the $ee\mu$ channel and the three subsets of the $\mu\mu e$ channel. Simulated events are used to train the BDT to differentiate between WH and ZH signal events and all background events

(diboson, $t\bar{t}$, Z/γ^*, etc.). The $H \to ZZ$ signal is used in the training of the $\mu\mu e$ BDTs as well. In events without jets, jet variables are set to zero.

For each BDT, 150 decision trees were trained [14]. A random subset of the events are used to train each tree. For each decision tree, a random subset of 4 of the input variables are chosen to train against. We use the Gini index to decide how to split each node in a decision tree, and the maximum depth of 5 is allowed for each decision tree.

In each of the four channels, separate BDT is trained for each of the Higgs boson mass points between 100 and 200 GeV. One half of the MC events are used in the training and testing of the BDTs, with the remaining events saved for limit setting. As the $Z\gamma$ background is modeled using data and therefore is limited in statistics, we train the BDT using $Z\gamma$ events from ALPGEN MC reweighted to match the data driven background. When selecting variables as inputs, we consider the expected properties of Higgs boson decays vs. backgrounds. For example, in Z + jet events with a jet faking a lepton, we expect the jet fake to be recoiling against the Z, so the $\Delta\phi$ between the Z daughters and the other lepton will peak near π radians, but will be flat for our Higgs signal. From those variables expected to provide some discrimination, we select those variables with well modeled distributions and good separating power. We also try to select variables with that are relatively uncorrelated in the signal and background distributions. The variables used as inputs to the BDTs are listed below.

Figures 1 and 2 show the 12 distributions used in training the $ee\mu$ BDT method. These variables are

- invariant mass of the di-electron pair ($M_{e_1e_2}$);
- invariant mass of the trilepton system with the $\not\!\!E_T$, where the $\not\!\!E_T$ is assumed to have $\eta = 0$ ($M_{e_1e_2\mu\not\!\!E_T}$);
- minimum transverse mass between the $\not\!\!E_T$ and either electron (M_T^{min});
- transverse momentum for the trailing electron ($p_T^{e_2}$);
- transverse momentum of the di-electron pair ($p_T^{e_1e_2}$);
- transverse momentum of the di-electron pair with the muon ($p_T^{e_1e_2\mu}$);
- $\not\!\!E_T{}^{special}$;
- $\not\!\!E_T{}^{significance}$;
- opening angle in ϕ between the di-electron pair ($\Delta\phi_{e_1,e_2}$);
- opening angle in ϕ between the di-electron system and the muon ($\Delta\phi_{e_1e_2,\mu}$);
- opening angle in η and ϕ space between the closest two leptons ($min(\Delta\mathcal{R}_{\ell_i,\ell_j})$);
- opening angle in η and ϕ space between the second closest two leptons ($med(\Delta\mathcal{R}_{\ell_i,\ell_j})$).

Figures $3-5$ show the 16 distributions used in training the $\mu\mu e$ BDT for the non-Z subset. The variables used are

- the invariant mass of the leading muon and electron ($M_{\mu_1 e}$);
- invariant mass of the di$-$muon pair and electron ($M_{\mu_1\mu_2 e}$);
- transverse momentum of the electron (p_T^e);
- transverse momentum of the di-muon pair ($p_T^{\mu_1\mu_2}$);
- pseudorapidity of the sum of the four-vectors of the three leptons in the lab frame ($\eta_{\mu_1\mu_2 e}$);
- scalar sum of the three leptons' transverse momenta plus the $\not\!\!E_T$ ($\sum_i p_T^i + \not\!\!E_T$);
- $\not\!\!E_T{}^{significance}$;
- $\not\!\!E_T{}^{special}$;
- the minimum transverse mass between the $\not\!\!E_T$ and any of the 3 leptons ($min((M_T^{\mu_1,\not\!\!E_T}, M_T^{\mu_2,\not\!\!E_T}, M_T^{e,\not\!\!E_T}))$);

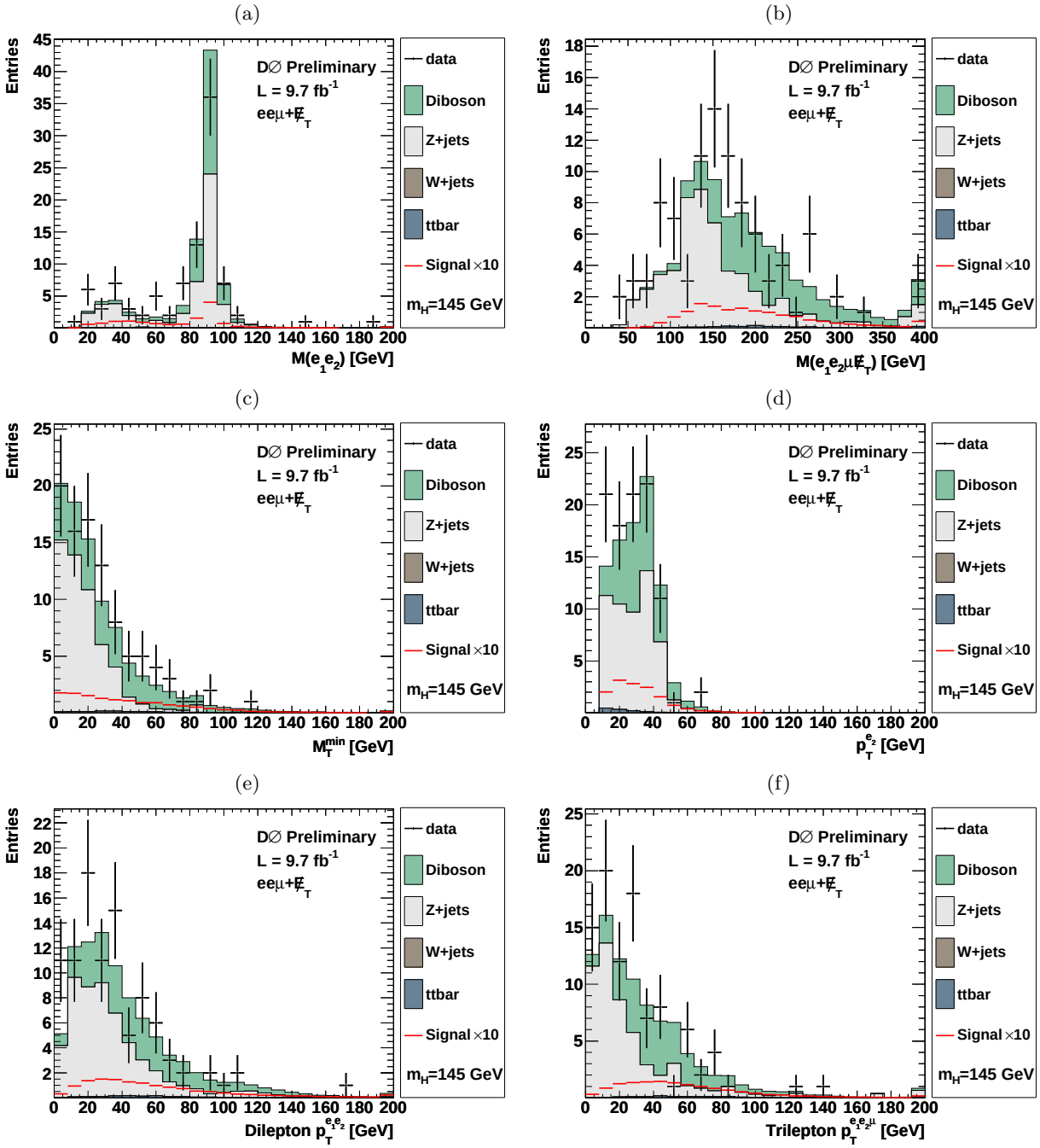

FIG. 1: The (a) di-electron mass, (b) trilepton + $\not\!\!E_T$ mass, (c) minimum transverse mass between either electron and the $\not\!\!E_T$, (d) transverse momentum of the trailing electron, (e) transverse momentum of the di-electron system, and (f) transverse momentum of the trilepton system. The expected signal, multiplied by 10, for a 145 GeV SM Higgs boson is shown. The highest bin includes all events above the upper range of the histogram (b).

- mt2 maximum - the "mt2" variable was proposed in Ref. [15], is similar to the transverse mass, but extended to a final state with two visible particles and two invisible ones. We compute the variable as in Ref. [16], using an algorithm provided by the authors. Because we have three visible particles in our final state, we calculate three mt2 variables, one for each combination. We order the three mt2 values, and use the highest value in the discriminant;

- opening angle in η and ϕ space between the closest two leptons ($min(\Delta\mathcal{R}_{\ell_i,\ell_j})$);

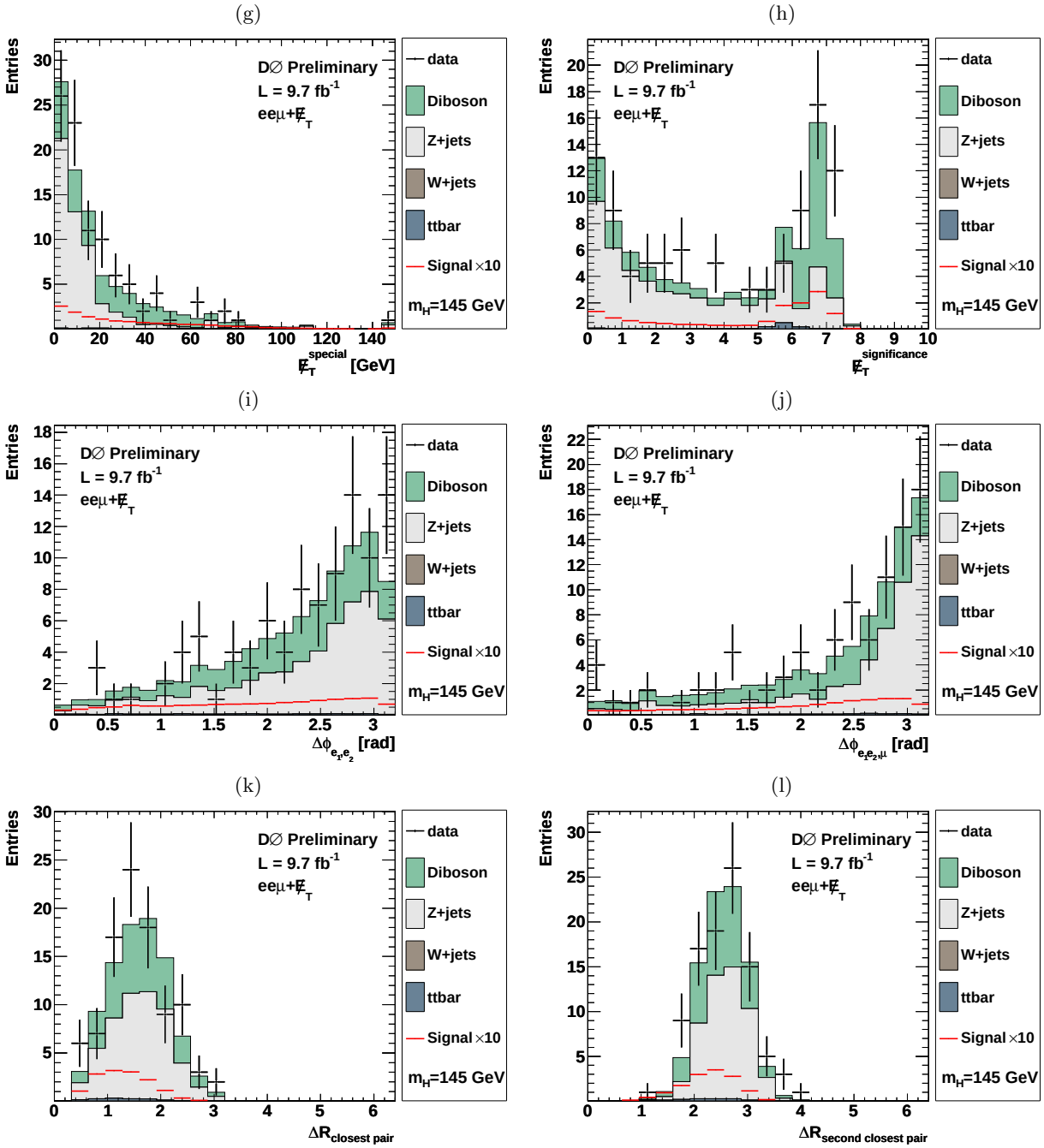

FIG. 2: The (g) $\not\!\!E_T{}^{special}$, (h) $\not\!\!E_T{}^{significance}$, (i) $\Delta\phi$ between the two electrons, (j) $\Delta\phi$ between di-electron system and the muon, (k) $\Delta\mathcal{R}$ between the closest two leptons, and (l) $\Delta\mathcal{R}$ between the second closest two leptons. The expected signal, multiplied by 10, for a 145 GeV SM Higgs boson is shown. The highest bin includes all events above the upper range of the histogram (h).

- opening angle in η and ϕ space between the second closest two leptons ($med(\Delta\mathcal{R}_{\ell_i,\ell_j})$);
- opening angle in ϕ between the di−muon system and the electron ($\Delta\phi_{\mu_1\mu_2,e}$);
- opening angle in ϕ between the two muons;
- product of the charges of the two muons ($q_{\mu_1} \times q_{\mu_2}$);

- transverse momentum of the leading jet, vertex confirmation not required ($p_T^{j_1}$).

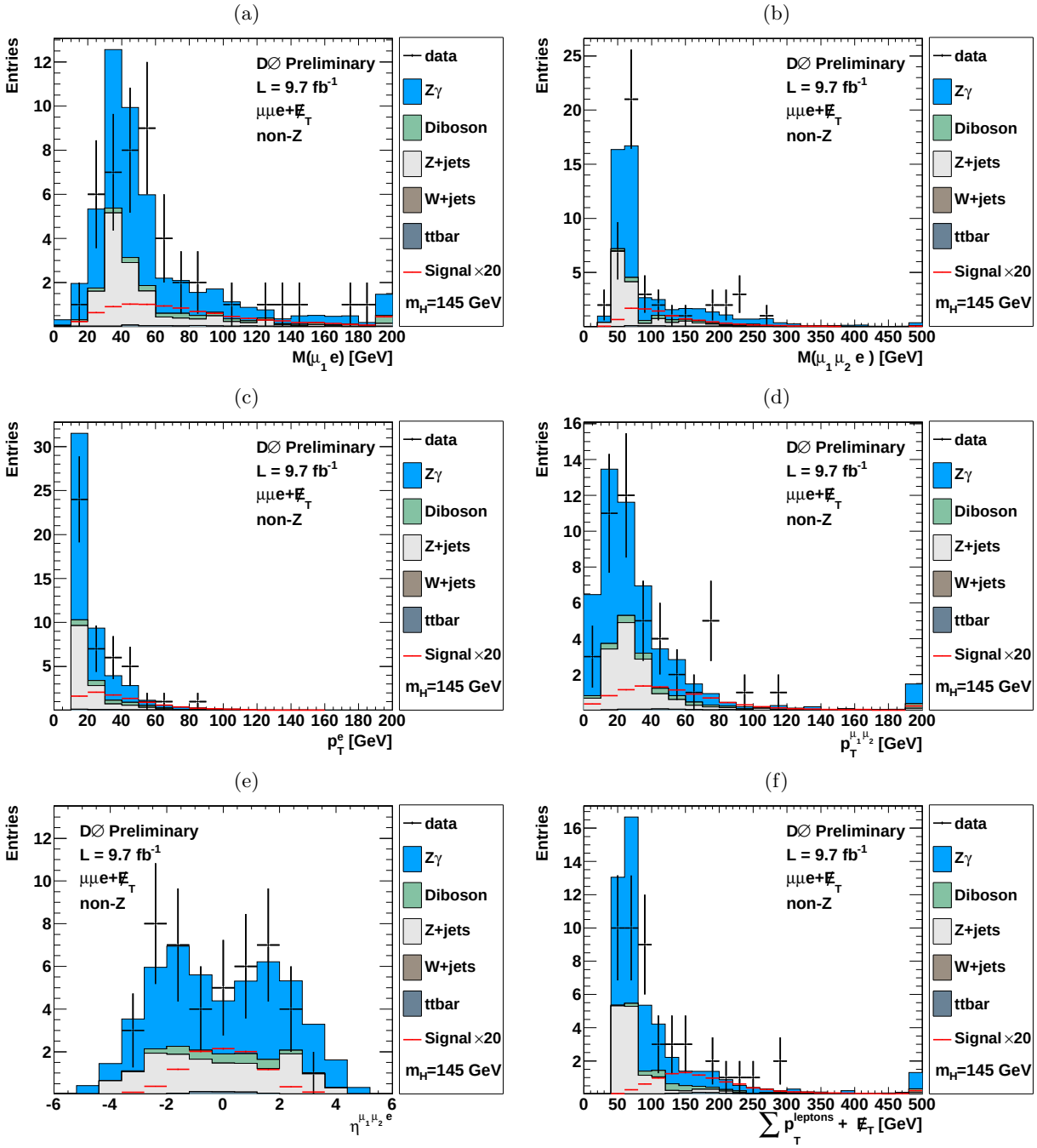

FIG. 3: Inputs to the BDTs for the non-Z $\mu\mu e$ subset. The (a) lead muon + electron mass, (b) trilepton mass, (c) transverse momentum of the electron, (d) transverse momentum of the di-muon pair, (e) physics pseudorapidity of the trilepton system, and (f) scalar sum of the leptons' p_Ts and $\not\!\!E_T$. The expected signal, multiplied by 20, for a 145 GeV SM Higgs boson is shown. The highest bin includes all events above the upper range of the histogram.

Figures 6 − 8 show the 16 distributions used in the $\mu\mu e$ BDT for the $Z + \not\!\!E_T{}^{significance}$ subset. These variables are

- the di−muon invariant mass ($M_{\mu_1\mu_2}$);
- transverse momentum of the electron (p_T^e);

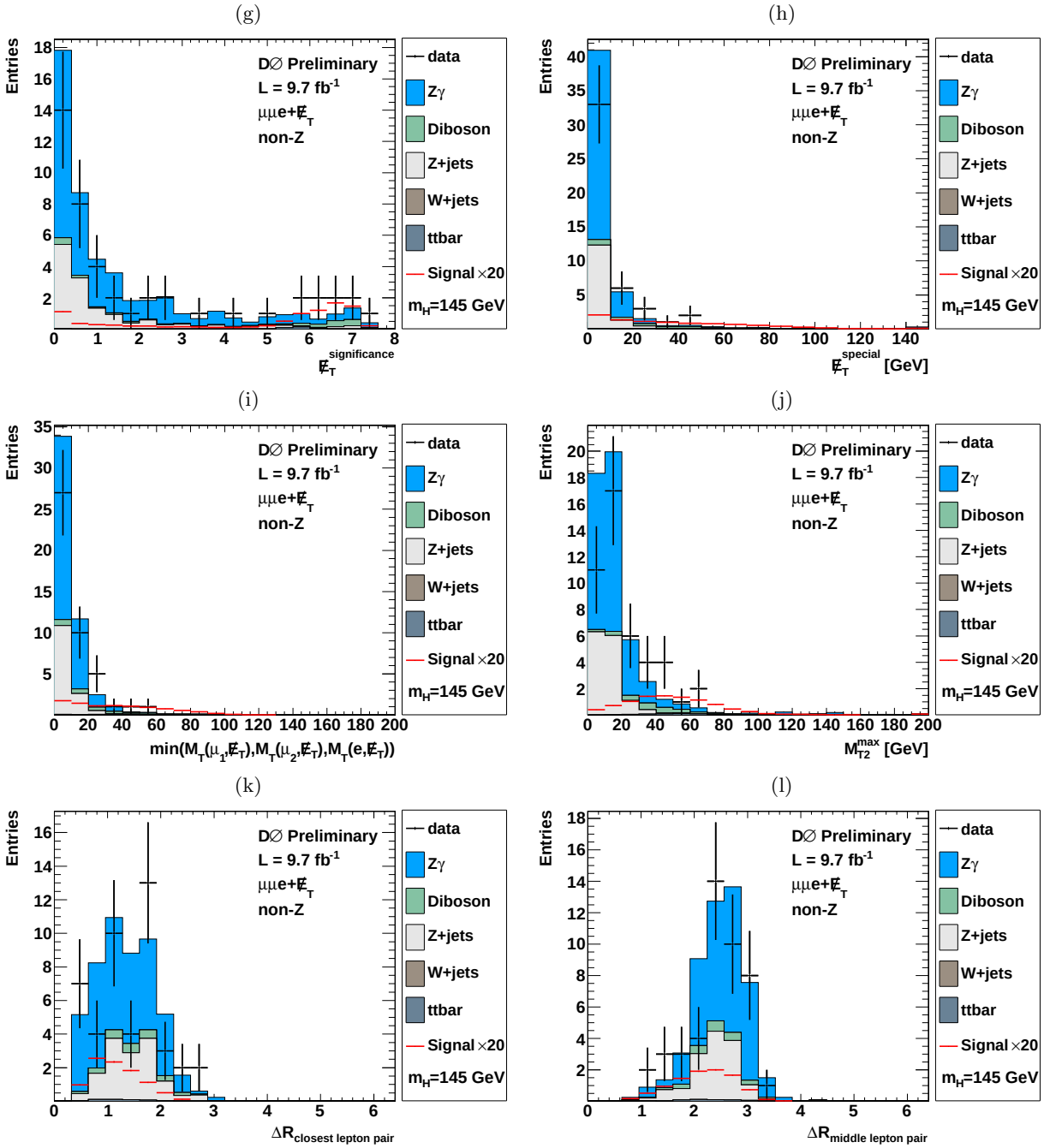

FIG. 4: Inputs to the BDTs for the non-Z $\mu\mu e$ subset. The (g) $\not\!\!E_T{}^{significance}$, (h) $\not\!\!E_T{}^{special}$, (i) lowest transverse mass between any lepton and the $\not\!\!E_T$(j) highest lowest mt2 transverse mass, (k) $\Delta\mathcal{R}$ between the closest two leptons, and (l) $\Delta\mathcal{R}$ between the second closest two leptons,. The expected signal, multiplied by 20, for a 145 GeV SM Higgs boson is shown. The highest bin includes all events above the upper range of the histogram.

- transverse momentum of the di-muon pair ($p_T^{\mu_1\mu_2}$);
- pseudorapidity of the sum of the four-vectors of the three leptons in the lab frame ($\eta_{\mu_1\mu_2 e}$);
- scalar sum of the three leptons' transverse momenta plus the $\not\!\!E_T$ ($\sum_i p_T^i + \not\!\!E_T$);
- $\not\!\!E_T{}^{significance}$;

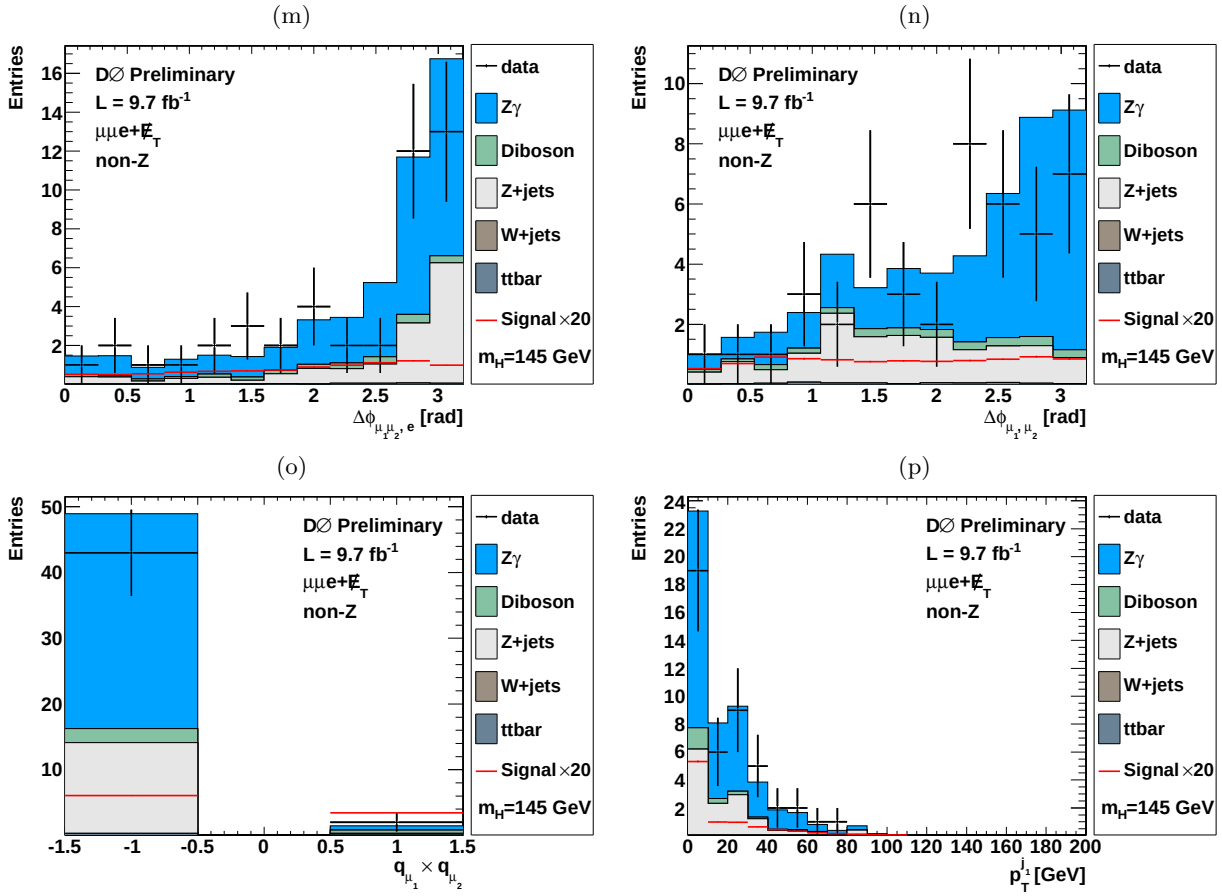

FIG. 5: Inputs to the BDTs for the non-Z $\mu\mu e$ subset. The (m) $\Delta\phi$ between di-muon system and the electron, (n) $\Delta\phi$ between the two muons, (o) product of electrical charges of the di-muon system, and (p) the transverse momentum of the leading jet in the event, without requiring vertex confirmation. For events without a jet, the jet p_T is set to zero. The expected signal, multiplied by 20, for a 145 GeV SM Higgs boson is shown. The highest bin includes all events above the upper range of the histogram.

- $\not\!\!E_T{}^{special}$;
- transverse mass between the $\not\!\!E_T$ and the electron ($M_T^{(e,\not\!\!E_T)}$);
- mt2 maximum - the highest value of mt2 between any 2 of the 3 leptons in the event and the $\not\!\!E_T$;
- opening angle in η and ϕ space between the closest two leptons ($min(\Delta\mathcal{R}_{\ell_i,\ell_j})$);
- minimum opening angle in ϕ between the $\not\!\!E_T$ and either the leading or trailing muon ($min(\Delta\phi_{\mu_1,\not\!\!E_T}, \Delta\phi_{\mu_2,\not\!\!E_T})$);
- opening angle in ϕ between the di$-$muon system and the electron ($\Delta\phi_{\mu_1\mu_2,e}$);
- opening angle in ϕ between the two muons;
- the number of vertex confirmed jets (N_{jets}^{vconf});
- the maximum opening angle in ϕ between the $\not\!\!E_T$ and any vertex confirmed jet ($max(\Delta\phi_{j^{vconf},\not\!\!E_T})$);
- transverse momentum of the leading vertex confirmed jet ($p_T^{j_1^{vconf}}$).

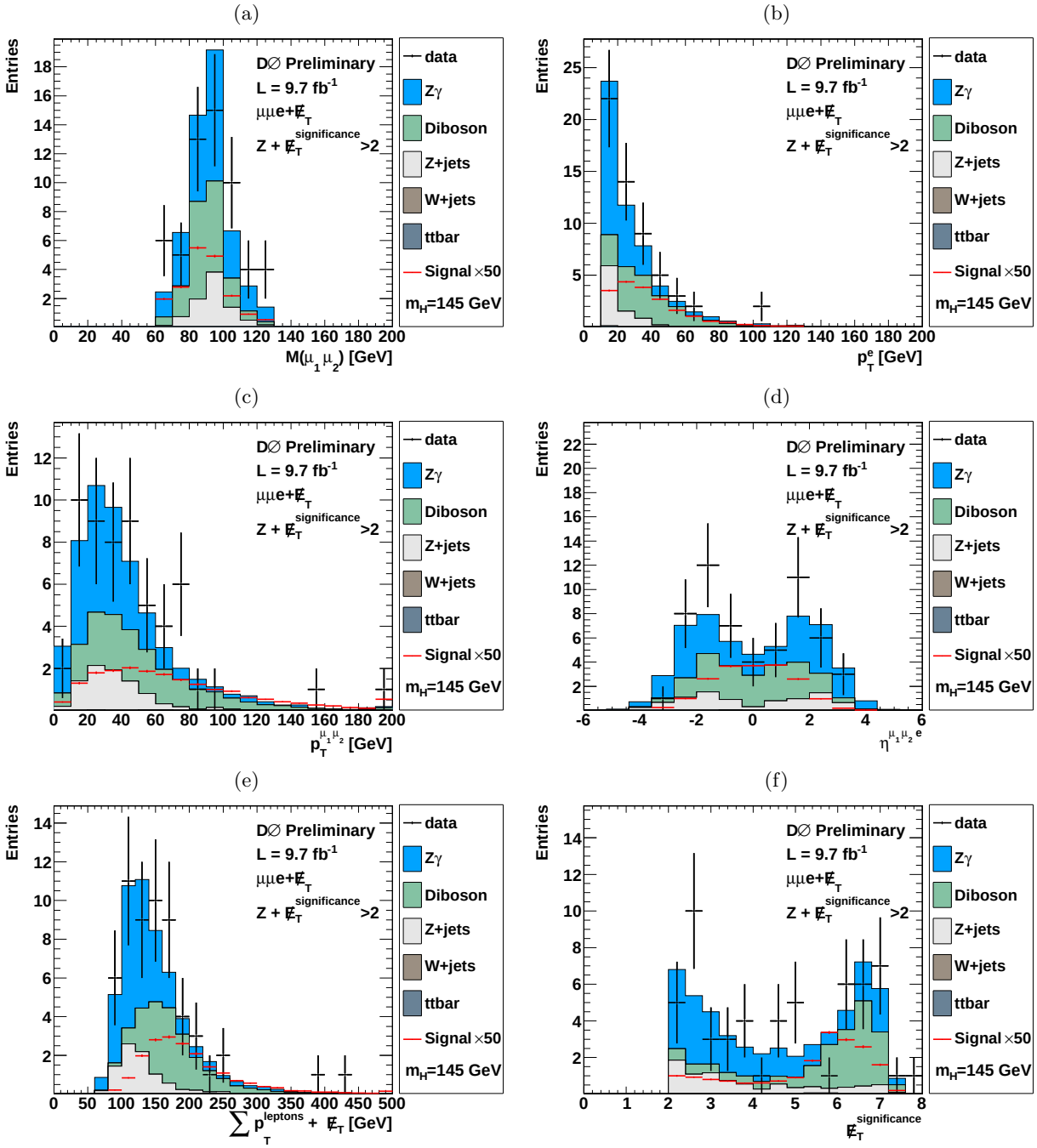

FIG. 6: Inputs to the BDTs for the $Z + \not\!\!E_T{}^{significance}$ $\mu\mu e$ subset. The (a) di-muon mass, (b) transverse momentum of the electron, (c) transverse momentum of the di-muon pair, (d) physics pseudorapidity of the trilepton system, (e) scalar sum of the leptons' p_Ts and $\not\!\!E_T$, and (f) $\not\!\!E_T{}^{significance}$, The expected signal, multiplied by 50, for a 145 GeV SM Higgs boson is shown. The highest bin includes all events above the upper range of the histogram.

VI. SYSTEMATIC UNCERTAINTIES

We consider two broad categories of uncertainties - those that change the overall normalization and those that can change the normalization and shape.

To account for the lepton identification efficiencies, a 2.5%(4%) systematic is applied for each electron(muon) in the final state. A PDF uncertainty of 2.5% [17] and a trigger efficiency uncertainty of 3.5% is applied to both the signal and background MC samples. We assign a 6.2% theoretical cross section uncertainty to the associated production (VH)

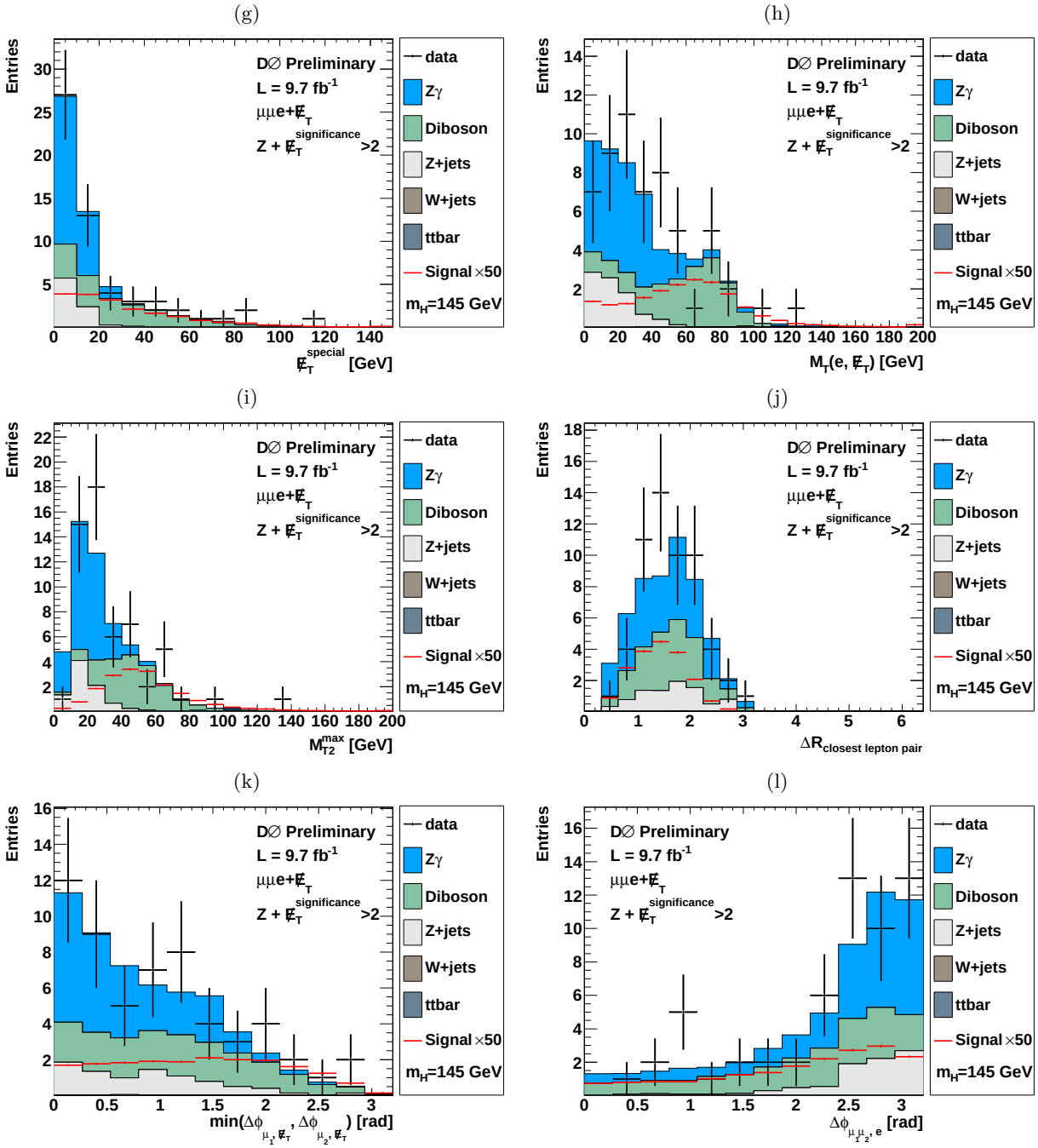

FIG. 7: Inputs to the BDTs for the $Z + \not\!\!E_T{}^{significance}$ $\mu\mu e$ subset. The (g) $\not\!\!E_T{}^{significance}$, (h) transverse mass between the electron and the $\not\!\!E_T$, (i) highest mt2 transverse mass, (j) $\Delta\mathcal{R}$ between the closest two leptons, (k) minimum $\Delta\phi$ between either muon and the $\not\!\!E_T$, and (l) $\Delta\phi$ between di-muon system and the electron. The expected signal, multiplied by 50, for a 145 GeV SM Higgs boson is shown. The highest bin includes all events above the upper range of the histogram.

signals, a 5% cross section uncertainty to the gluon-gluon fusion ($ggH, H \to VV$) signals, and a 4.9% uncertainty on the vector boson fusion (VBF) signal [5]. A 6% theoretical cross section uncertainty is applied to the diboson background MC [10], while a 7% uncertainty is added to the $t\bar{t}$ sample [11]. The theoretical cross section uncertainty for the $Z+$ jets and $W+$ jets backgrounds are estimated to be $\pm$6% [10] each with an additional 30% uncertainty on these samples due to the uncertainty on the jet to lepton fake rate. A 9.5% uncertainty is applied to the $Z\gamma$ background due to the reweighting described in Section III. This uncertainty is based on the statistical uncertainty

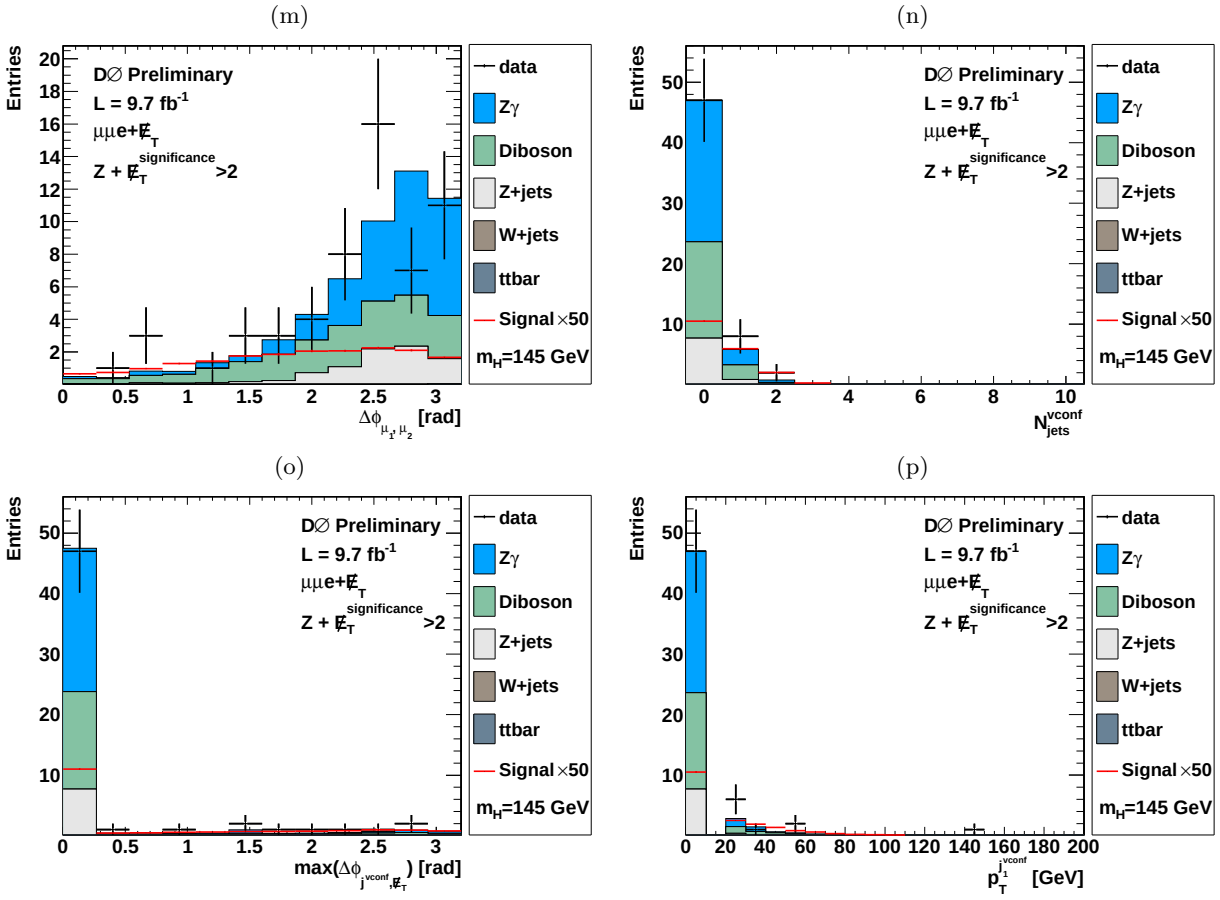

FIG. 8: Inputs to the BDTs for the $Z + \not\!\!E_T{}^{significance}$ $\mu\mu e$ subset. The (m) $\Delta\phi$ between the two muons, (n) number of vertex confirmed jets, (o) largest opening angle between the $\not\!\!E_T$and any vertex confirmed jet, and (p) the transverse momentum of the highest p_T vertex confirmed jet in the event. Events with no jets have the jet quantities set to zero. The expected signal, multiplied by 50, for a 145 GeV SM Higgs boson is shown. The highest bin includes all events above the upper range of the histogram.

Figures $9 - 11$ show the 16 distributions used in the $\mu\mu e$ BDT for the $Z +$ no $\not\!\!E_T{}^{significance}$ subset. These variables are

- the di−muon invariant mass ($M_{\mu_1\mu_2}$);
- invariant mass of the di−muon pair and electron ($M_{\mu_1\mu_2 e}$);
- transverse momentum of the electron (p_T^e);
- transverse momentum of the leading muon ($p_T^{\mu_1}$);
- transverse momentum of the di−muon pair with the electron ($p_T^{\mu_1\mu_2 e}$);
- pseudorapidity of the sum of the four-vectors of the three leptons in the lab frame ($\eta_{\mu_1\mu_2 e}$);
- scalar sum of the three leptons' transverse momenta plus the $\not\!\!E_T$ $(\sum_i p_T^i + \not\!\!E_T)$;
- opening angle in η and ϕ space between the closest two leptons ($min(\Delta\mathcal{R}_{\ell_i,\ell_j})$);
- opening angle in η and ϕ space between the second closest two leptons ($med(\Delta\mathcal{R}_{\ell_i,\ell_j})$);
- opening angle in η and ϕ space between the farthest two leptons ($max(\Delta\mathcal{R}_{\ell_i,\ell_j})$);
- opening angle in ϕ between the di−muon system and the electron ($\Delta\phi_{\mu_1\mu_2,e}$);
- opening angle in ϕ between the two muons;
- the number of vertex confirmed jets (N_{jets}^{vconf});
- the maximum opening angle in ϕ between the $\not\!\!E_T$ and any vertex confirmed jet ($max(\Delta\phi_{j^{vconf},\not\!\!E_T})$);
- transverse momentum of the leading jet, vertex confirmation not required ($p_T^{j_1}$);
- pseudorapidity of the leading jet, vertex confirmation not required (η^{j_1});
- fraction of tracks associated with the leading jet that point back to the same interaction point as the 3 leptons, no vertex confirmation required.

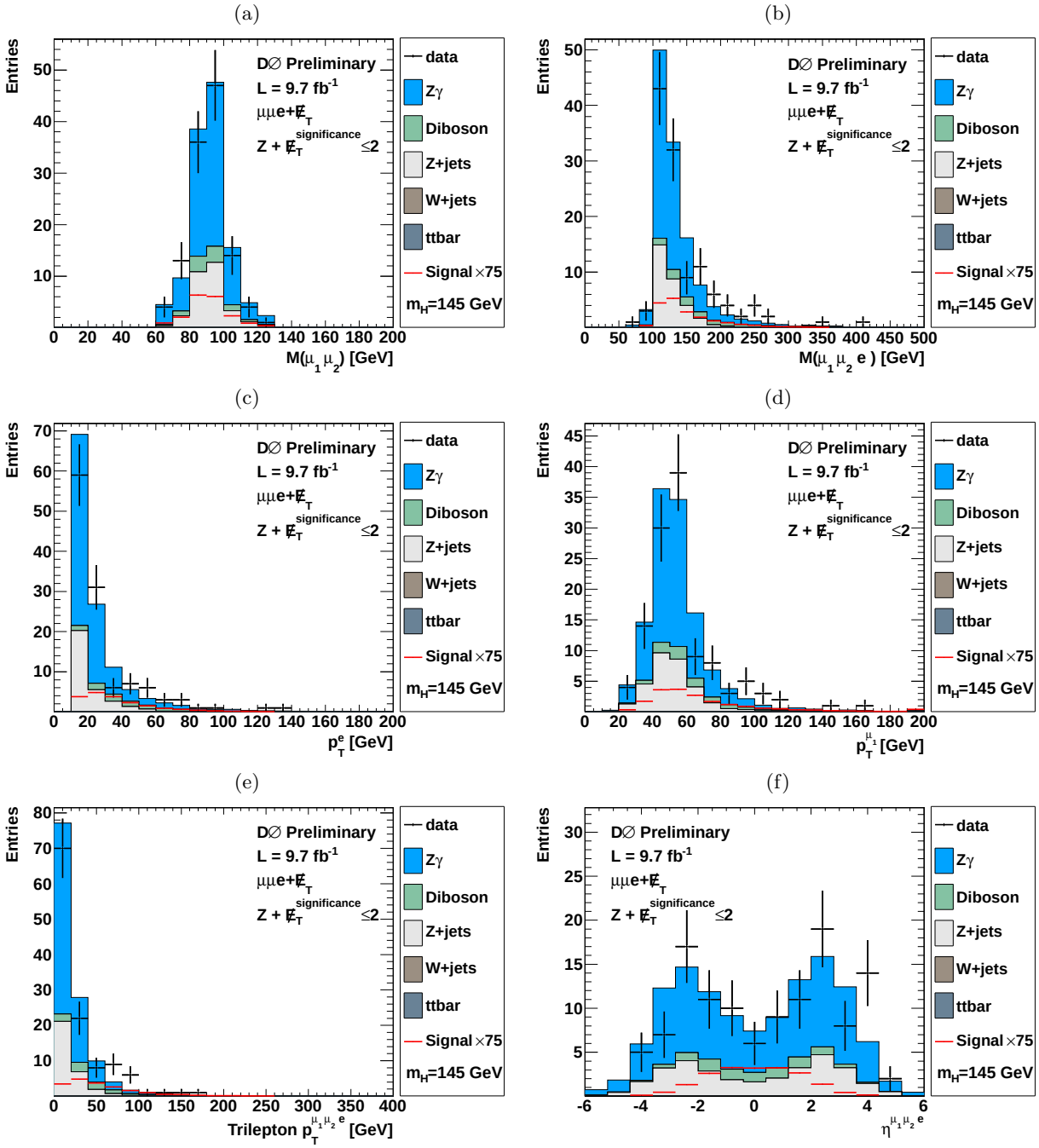

FIG. 9: Inputs to the BDTs for the Z + no $\not\!\!E_T{}^{significance}$ $\mu\mu e$ subset. The (a) di-muon mass, (b) trilepton mass, (c) transverse momentum of the electron, (d) transverse momentum of the leading muon, (e) transverse momentum of the di-muon pair with the electron, and (f) physics pseudorapidity of the trilepton system. The expected signal, multiplied by 75, for a 145 GeV SM Higgs boson is shown. The highest bin includes all events above the upper range of the histogram.

of the fake ratio and estimated jet contamination of the background. The luminosity uncertainty has been measured to be to be 6.1% [18].

An uncertainty in the shape of the $Z-p_T$ reweighting distributions is calculated by shifting the reweighting function by $\pm 1\sigma$. The electron p_T resolution is estimated by applying the $\pm 1\sigma$ variation the electron p_T uncertainty. Similarly, the muon p_T resolution is estimated by applying the $\pm 1\sigma$ variation in the muon p_T uncertainty.

In the $\mu\mu e$ final state, we additionally calculate systematic uncertainties on jet reconstruction. The jet energy scale uncertainty is estimated by modifying the shifting corrections by $\pm 1\sigma$ their uncertainties and then shifting. The

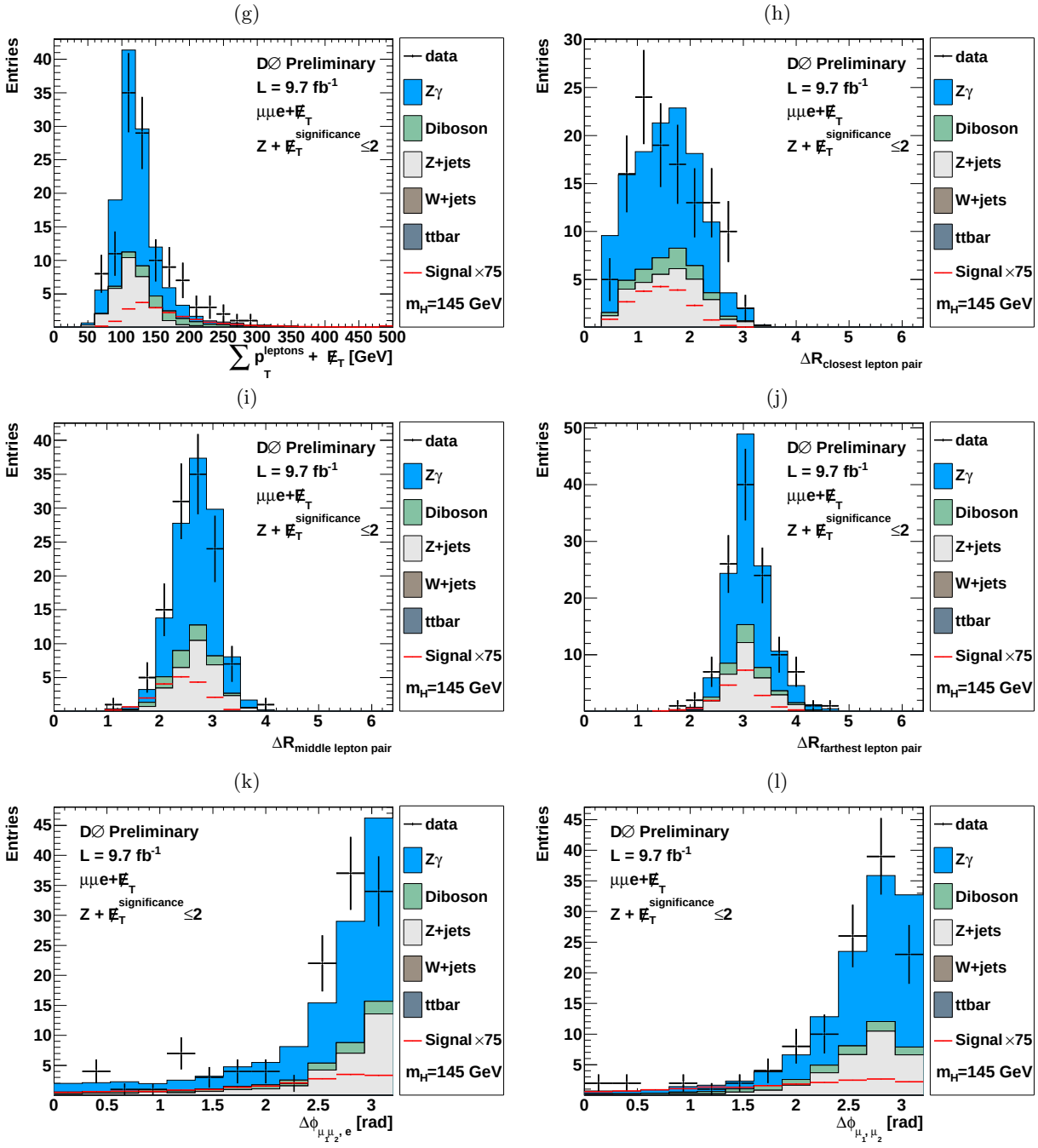

FIG. 10: Inputs to the BDTs for the Z + no $\not\!\!E_T{}^{significance}$ $\mu\mu e$ subset. The (g) scalar sum of the leptons' p_Ts and $\not\!\!E_T$, (h) $\Delta\mathcal{R}$ between the closest two leptons, (i) $\Delta\mathcal{R}$ between the second closest two leptons, (j) $\Delta\mathcal{R}$ between the farthest two leptons (k) $\Delta\phi$ between di-muon system and the electron, and (l) $\Delta\phi$ between the two muons. The expected signal, multiplied by 75, for a 145 GeV SM Higgs boson is shown. The highest bin includes all events above the upper range of the histogram.

jet resolution is calculated by varying the jet resolution by 1σ. The jet identification uncertainty is calculated by decreasing jet efficiency by 1σ. The vertex confirmation uncertainty is calculated by decreasing the vertex confirmation efficiency by 1σ.

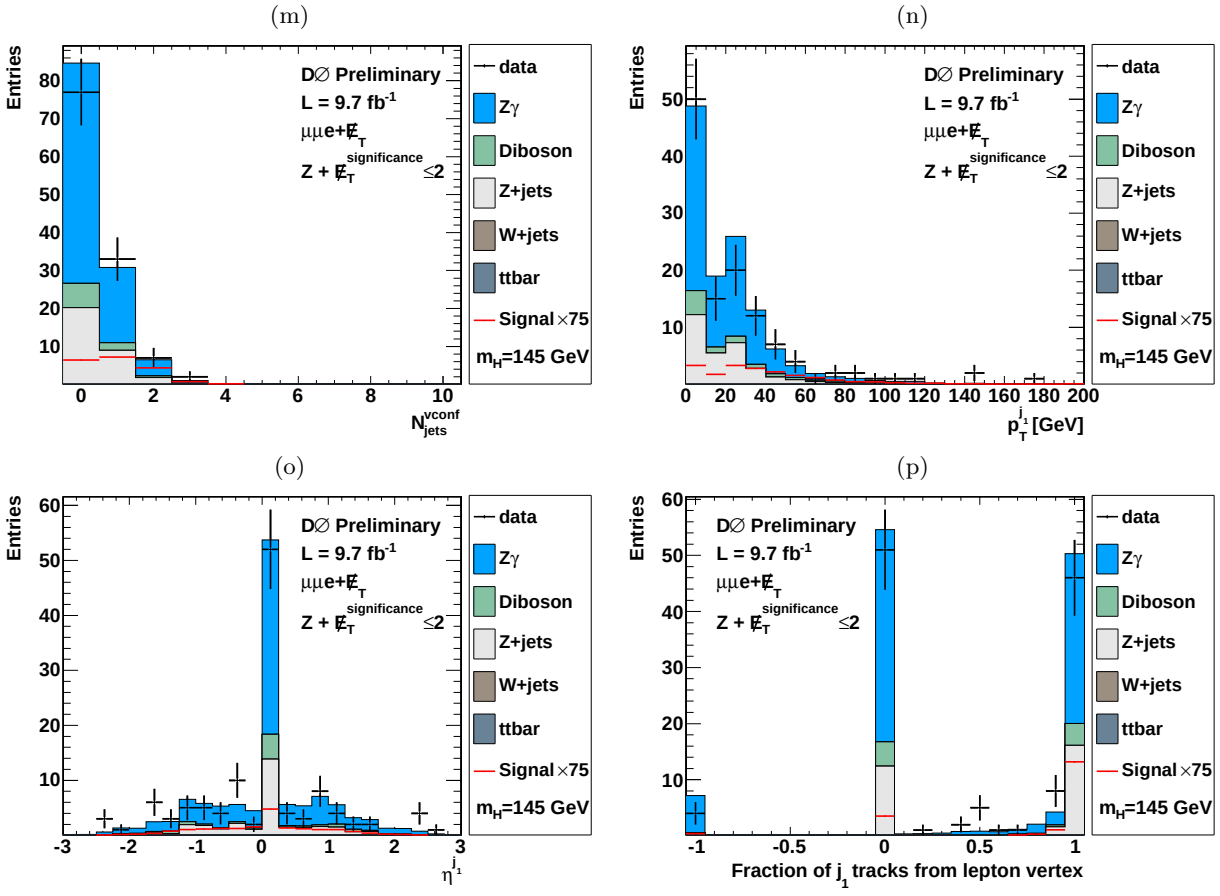

FIG. 11: Inputs to the BDTs for the Z + no $\not\!\!E_T{}^{significance}$ $\mu\mu e$ subset. The (m) number of vertex confirmed jets, (n) transverse momentum of the leading jet in the event, without requiring vertex confirmation, (o) pseudorapidity of the leading jet in the event, without requiring vertex confirmation, and (p) fraction of tracks associated with the leading jet that point back to the same interaction point as the 3 leptons, no vertex confirmation required (jets with no tracks set to -1). The expected signal, multiplied by 75, for a 145 GeV SM Higgs boson is shown. Events with no jets have the jet quantities set to zero. The highest bin includes all events above the upper range of the histogram.

VII. RESULTS AND SUMMARY

We see that the BDT output distributions in data agree within uncertainties with the expected backgrounds, as shown in Figure 12. The BDT output distributions for each mass point are therefore used to set limits on the Higgs boson inclusive production cross section, $\sigma(p\bar{p} \to H + X)$, assuming SM values for the branching ratios and for the relative cross sections of the various Higgs boson production mechanisms considered. We calculate the limits using a modified frequentist method (CLs), with a log-likelihood ratio (LLR) test statistic [19]. The $ee\mu$ and three $\mu\mu e$ channels are combined in the limit, but to achieve maximal sensitivity, the individual inputs are treated separately by the limit setting software. To minimize the degrading effects of systematics on the search sensitivity, the individual background contributions are fitted to the data observation by maximizing a profile likelihood function for the background-only and signal-plus-background hypotheses [20].

Table II presents expected and observed upper limits at 95% CL for $\sigma(p\bar{p} \to H + X)$ relative to that expected in the SM for each Higgs boson mass considered. Figure 13 shows the expected and observed limits for $\sigma(p\bar{p} \to H + X)$ relative to the SM for the different Higgs boson masses, while Figure 14 shows the corresponding LLR distribution.

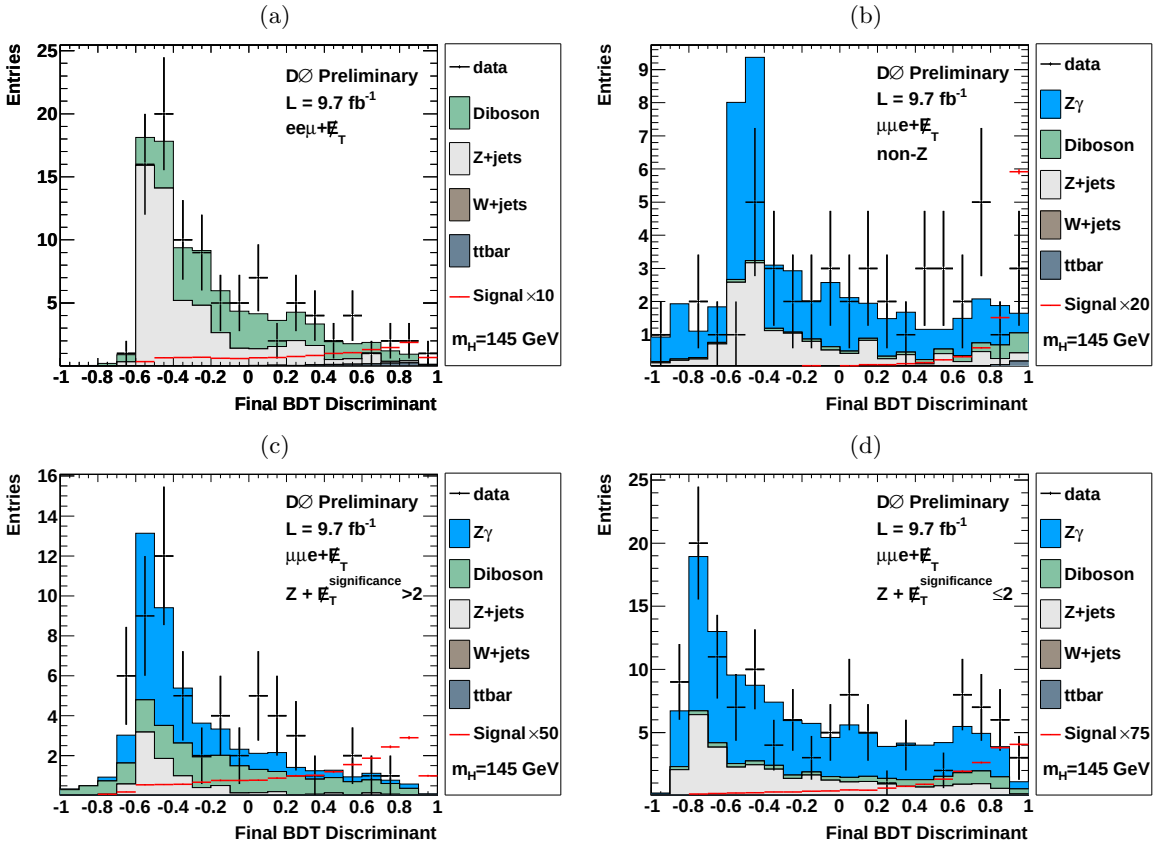

FIG. 12: Final BDT discriminant for (a) $ee\mu$ channel, (b) $\mu\mu e$ channel, non-Z subset, (c) $\mu\mu e$ channel, $Z + \not\!\!E_T{}^{significance}$ subset, and (d) $\mu\mu e$ channel, Z no $\not\!\!E_T{}^{significance}$ subset. The discriminant shown is trained for a Higgs boson mass of 145 GeV.

TABLE II: Expected and observed upper limits at 95% CL for $\sigma(p\bar{p} \to H + X)$ relative to the SM for the total combination and separately for the $ee\mu$ and $\mu\mu e$ channels in Run II for different Higgs boson masses (m_H). The $\mu\mu e$ channel result is for the 3 $\mu\mu e$ subsets combined.

m_H (GeV/c^2)	100	105	110	115	120	125	130	135	140	145	150
Exp. all	13.97	14.77	14.51	14.52	12.40	11.07	9.16	7.60	7.68	6.60	6.55
Obs. all	35.32	39.44	28.59	26.97	21.50	19.29	21.24	14.98	13.77	11.16	9.59
Exp. $ee\mu$	19.09	19.84	20.29	18.30	16.03	15.28	12.29	10.81	10.27	9.54	9.16
Obs. $ee\mu$	36.22	40.97	30.83	29.11	24.94	22.24	19.23	16.06	13.82	14.17	11.97
Exp. $\mu\mu e$	22.52	22.96	22.44	23.82	21.59	16.86	14.60	13.44	11.75	10.50	10.13
Obs. $\mu\mu e$	51.32	55.84	41.48	41.66	30.44	27.34	34.67	22.82	22.72	15.31	14.89

m_H (GeV/c^2)	155	160	165	170	175	180	185	190	195	200
Exp. all	6.25	6.47	6.64	6.87	7.99	8.35	9.23	9.98	11.74	11.66
Obs. all	9.01	9.97	7.13	8.83	9.15	13.36	10.51	15.14	13.70	19.29
Exp. $ee\mu$	9.13	9.70	9.73	10.35	11.98	13.31	13.83	15.45	16.35	17.80
Obs. $ee\mu$	11.79	11.73	11.75	11.46	12.36	13.59	15.29	13.64	13.79	16.69
Exp. $\mu\mu e$	10.00	10.23	10.84	10.71	12.25	12.10	13.84	14.98	17.40	16.88
Obs. $\mu\mu e$	14.16	16.39	10.30	14.99	15.89	23.89	16.06	30.32	28.60	35.62

VIII. CONCLUSION

A search for the standard model (SM) Higgs boson was presented using a trilepton sample in $p\bar{p}$ collisions at a center-of-mass energy of $\sqrt{s} = 1.96$ TeV with data collected from April 2002 to September 2011 by the RunII DØ detector corresponding to 9.7 fb^{-1} of integrated luminosity. No significant excess is observed above the SM background and limits are extracted on the SM Higgs boson production cross section for a Higgs boson masses between 100 and 200 GeV, in intervals of 5 GeV.

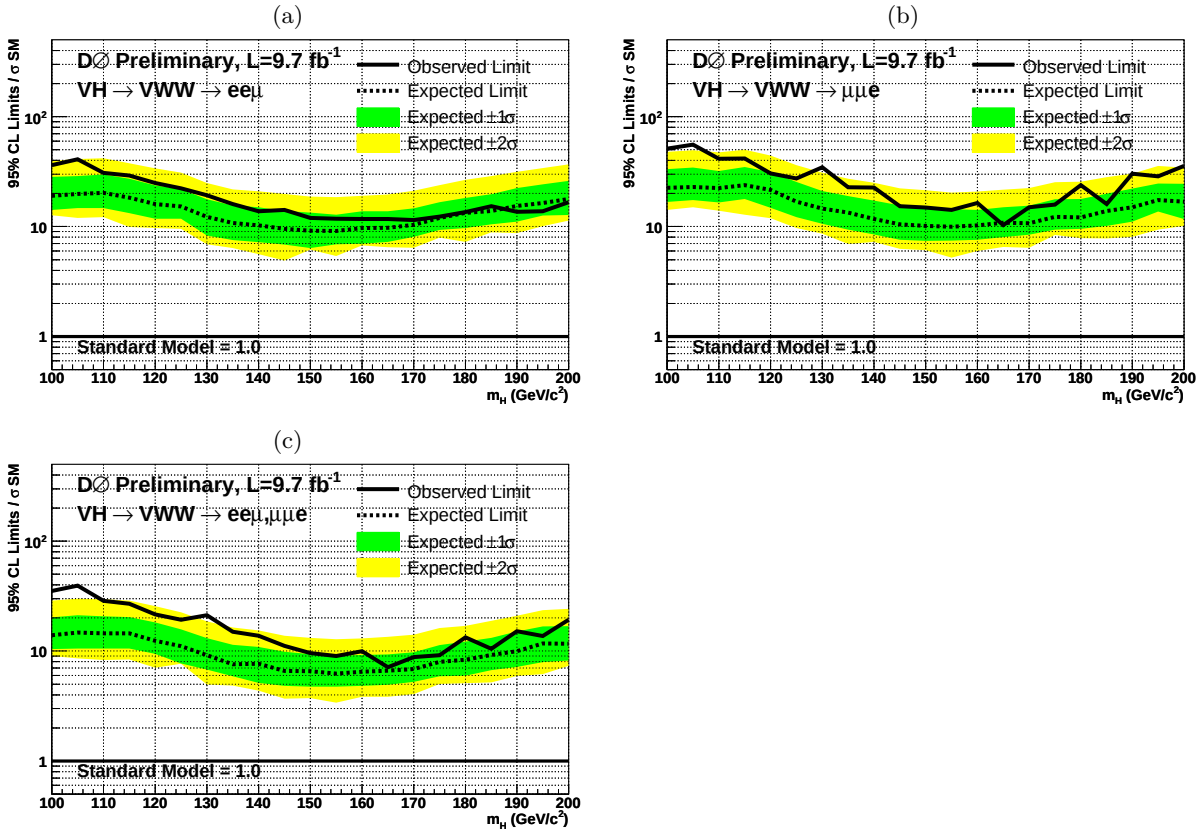

FIG. 13: Excluded cross section $\sigma(p\bar{p} \to H + X)$ at 95% CL in units of the SM cross section as a function of m_H using (a) $ee\mu$ channel, (b) $\mu\mu e$ channel, and (c) combined channels.

Acknowledgments

We thank the staffs at Fermilab and collaborating institutions, and acknowledge support from the DOE and NSF (USA); CEA and CNRS/IN2P3 (France); MON, Rosatom and RFBR (Russia); CNPq, FAPERJ, FAPESP and FUNDUNESP (Brazil); DAE and DST (India); Colciencias (Colombia); CONACyT (Mexico); NRF (Korea); FOM (The Netherlands); STFC and the Royal Society (United Kingdom); MSMT and GACR (Czech Republic); BMBF and DFG (Germany); SFI (Ireland); The Swedish Research Council (Sweden); and CAS and CNSF (China).

[1] V.M. Abazov *et al.* [DØ Collaboration], Nucl. Instr. and Methods A **565**, 463 (2006).
[2] R. Angstadt, *et al.*, Nucl. Instr. and Methods A **622**, 298 (2010).
[3] S. Abachi *et al.* [DØ Collaboration], Nucl. Instrum. and Methods A **338**, 185 (1994).
[4] V.M. Abazov *et al.*, Nucl. Instrum. and Methods A **552**, 372-398 (2005).
[5] The Tevatron New Phenomena and Higgs Working Group, FERMILAB, CDF Note 10806, D0 Note 6303, `http://www-d0.fnal.gov/Run2Physics/WWW/results/prelim/HIGGS/H129/H129.pdf`
[6] T. Sjöstrand *et al.*, Comput. Phys. Commun. **135**, 238 (2001);
we use version 6.323 or later.
[7] M.L. Mangano *et al.*, JHEP **0307**, 001 (2003);
we use version 2.11.
[8] V. M. Abazov *et al.*, Phys. Rev. Lett. **100**, 102002 (2008).
[9] R. Brun and F. Carminati, CERN Library Long Writeup, W5013, (1994).
[10] J. Campbell and R. K. Ellis, `http://mcfm.fnal.gov/`.
J. M. Campbell, R. K. Ellis, Nucl. Phys. Proc. Suppl. **205-206**, 10-15 (2010). [arXiv:1007.3492 [hep-ph]].
[11] U. Langenfeld, S. Moch and P. Uwer, Phys. Rev. D **80**, 054009 (2009).
[12] G. Blazey *et al.*, in *Proceedings of Physics at Run II: QCD and Weak Boson Physics Workshop: Final General Meeting*,

(a)

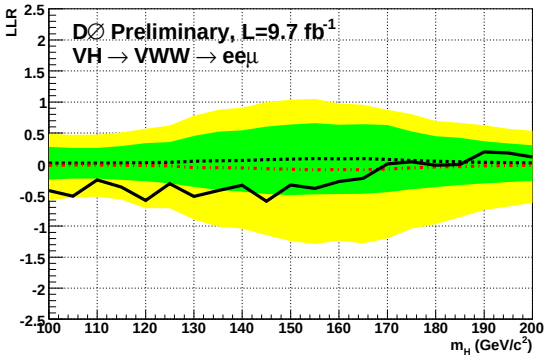

(b)

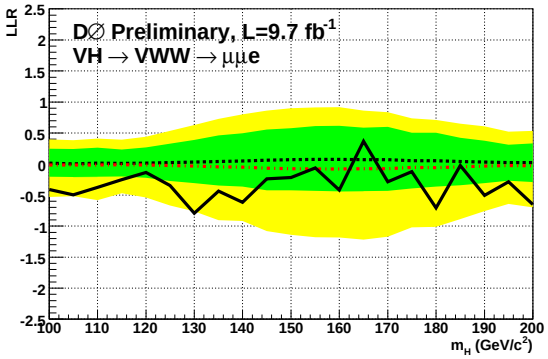

(c)

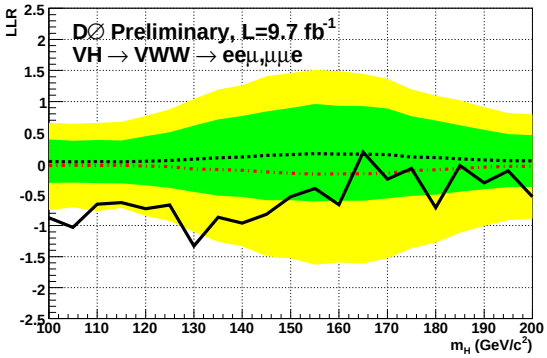

FIG. 14: The observed LLR (solid line) as a function of m_H using (a) $ee\mu$ channel, (b) $\mu\mu e$ channel, and (c) combined channels. Also shown are the expected LLRs for the background only (black dashed line) and signal + background (red dashed line) hypotheses, with the green and yellow bands indicating one and two sigma fluctuations of the expected LLR for the background-only hypothesis.

eds. U. Bauer, R. Ellis, arXiv: hep-ex/0005012 D. Zeppenfeld (Fermilab, Batavia, USA, 2000), p. 47.
[13] V. M. Abazov *et al.*, Phys. Rev. Lett. **101**, 241801 (2008).
[14] A. Hoecker *et al.*, arXiv:physics/0703039v5 [physics.data-an].
[15] C. Lester and D. Summers, Phys. Lett. B **463**, 99-103 (1999).
[16] H. Cheng and Z. Han, JHEP **12**, 063 (2008).
[17] A. D. Martin, W. J. Stirling, R. S. Thorne and G. Watt, Eur. Phys. J. C **63**, 189 (2009).
[18] T. Andeen *et al.*, FERMILAB-TM-2365 (2007).
[19] T. Junk, Nucl. Instrum. and Methods A **434**, 435 (1999).
A. Read, CERN 2000-005 (30 May 2000).
[20] W. Fisher, FERMILAB-TM-2386-E.